Nano Research

ISSN 1998-0124 CN 11-5974/O4
https://doi.org/10.26599/NR.2026.94909237

Research Article

Raman fingerprints of symmetry breaking and correlated electronic states in magic-angle twisted bilayer graphene

Yingzhuo Han[1], Junnan Jiang[2], Yingbo Wang[1], Kenji Watanabe[3], Takashi Taniguchi[4], Yuhang Jiang[2](✉), Jinhai Mao[1](✉)

[1] School of Physical Sciences, University of Chinese Academy of Sciences, Beijing 100049, China

[2] College of Materials Science and Optoelectronic Technology, Center of Materials Science and Optoelectronics Engineering, University of Chinese Academy of Sciences, Beijing 100049, China

[3] Research Center for Electronic and Optical Materials, National Institute for Materials Science, Tsukuba 305-0044, Japan

[4] International Center for Materials Nanoarchitectonics, National Institute for Materials Science, Tsukuba 305-0044, Japan

Nano Res., **Just Accepted Manuscript** • https://doi.org/10.26599/NR.2026.94909237

https://www.sciopen.com/journal/1998-0124 on Oct. 3, 2026

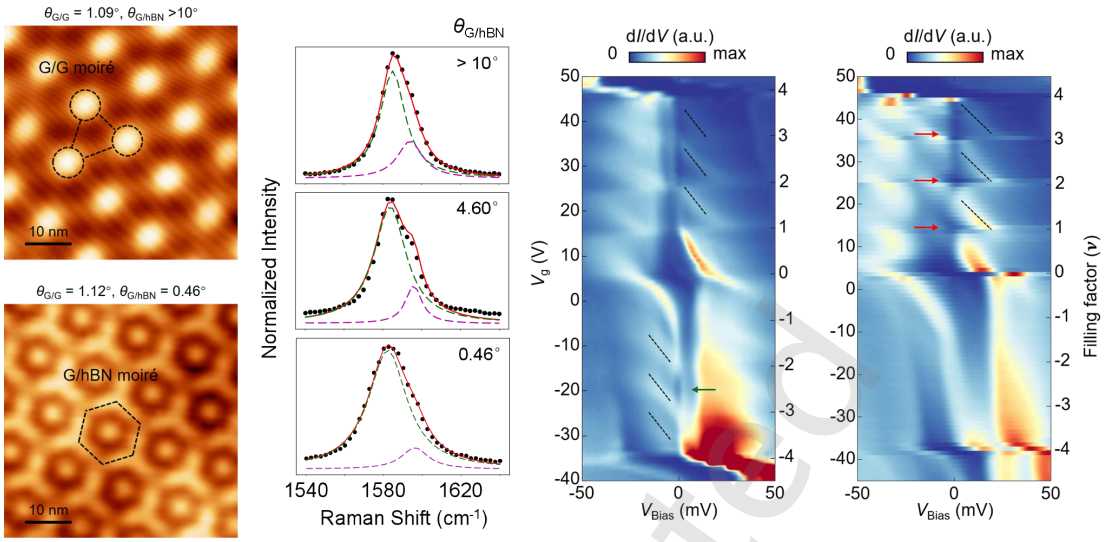
© The Authors(s)

Just Accepted

This is a "Just Accepted" manuscript, which has been examined by the peer-review process and has been accepted for publication. A "Just Accepted" manuscript is published online shortly after its acceptance,which is prior to technical editing and formatting and author proofing. Tsinghua University Press (TUP) provides "Just Accepted" as an optional and free service which allows authors to make their results available to the research community as soon as possible after acceptance. After a manuscript has been technically edited and formatted, and the page proofs have been corrected, it will be removed from the "Just Accepted" web site and published officially with volume and article number (e.g., *Nano Research*, **2025**, *18*, 94906990). Please note that technical editing may introduce minor changes to the manuscript text and/or graphics which may affect the content, and all legal disclaimers that apply to the journal pertain. In no event shall TUP be held responsible for errors or consequences arising from the use of any information contained in these "Just Accepted" manuscripts. To cite this anuscript please use its Digital Object Identifier (DOI®),which is identical for all formats of publication.

Just Accepted

TABLE OF CONTENTS



Raman spectroscopy reveals a systematic enhancement of the G-mode linewidth as magic-angle twisted bilayer graphene approaches alignment with hBN. Complementary STM/S measurements show that the same alignment conditions markedly modify the correlated electronic states.

Just Accepted

Raman fingerprints of symmetry breaking and correlated electronic states in magic-angle twisted bilayer graphene

Yingzhuo Han[1], Junnan Jiang[2], Yingbo Wang[1], Kenji Watanabe[3], Takashi Taniguchi[4], Yuhang Jiang[2] ✉, Jinhai Mao[1] ✉

1 School of Physical Sciences, University of Chinese Academy of Sciences, Beijing 100049, China

2 College of Materials Science and Optoelectronic Technology, Center of Materials Science and Optoelectronics Engineering, University of Chinese Academy of Sciences, Beijing 100049, China

3 Research Center for Electronic and Optical Materials, National Institute for Materials Science, Tsukuba 305-0044, Japan

4 International Center for Materials Nanoarchitectonics, National Institute for Materials Science, Tsukuba 305-0044, Japan

Received: 16 May 2026; **Revised:** 17 July 2026; **Accepted:** 24 July 2026

✉Address correspondence to Yuhang Jiang, yuhangjiang@ucas.ac.cn; Jinhai Mao, jhmao@ucas.ac.cn

Cite this article: *Nano Research*, 2026, 19, 94909237 https://doi.org/10.26599/NR.2026.94909237

ABSTRACT:

Magic-angle twisted bilayer graphene (MATBG) hosts ultra-flat bands and a variety of strongly correlated electronic phases that are highly sensitive to substrate alignment. However, a rapid and non-destructive method to identify both the magic angle and its structural alignment remains lacking. Here, we employ Raman spectroscopy to systematically investigate MATBG devices with different twist angles and graphene/hBN alignment conditions. We show that the Raman G peak linewidth (Γ_G) is significantly broadened near the magic angle due to flat-band–enhanced electron–phonon coupling. It becomes further enlarged when MATBG is aligned with hBN, reflecting additional symmetry breaking induced by the substrate moiré potential. Scanning tunneling microscopy and spectroscopy confirm the presence of flat bands and correlated electronic states, and demonstrate their strong dependence on hBN alignment. Our work establishes Raman spectroscopy as a powerful probe linking lattice symmetry, substrate alignment, and correlated electronic phases in moiré graphene systems.

KEYWORDS: magic-angle twisted bilayer graphene; Raman spectroscopy; moiré superlattice; symmetry breaking; correlated electronic states

Just Accepted

1 Introduction

The discovery of moiré superlattices in twisted van der Waals heterostructures has opened a powerful route for engineering electronic band structures through interlayer rotational alignment [1–4]. In twisted bilayer graphene (TBG), a small twist angle between two graphene layers generates a long-wavelength moiré potential that reconstructs the Dirac bands [5–7]. When the twist angle approaches the so-called magic angle (~1.1°), interlayer hybridization and moiré interference dramatically reduce the bandwidth, producing ultra-flat electronic bands with strongly enhanced density of states. These flat bands host a wide range of interaction-driven quantum phases, including correlated insulating states [8–13], unconventional superconductivity [14–17], and symmetry-broken electronic orders [18–21]. Owing to this exceptional tunability, magic-angle twisted bilayer graphene (MATBG) has emerged as a central platform for investigating strong correlations and emergent quantum phenomena in two-dimensional materials.

Precise identification of the twist angle and lattice symmetry is essential for understanding and controlling the correlated phases in MATBG. Raman spectroscopy provides a fast, non-destructive, and high-resolution probe of lattice vibrations and electron–phonon coupling, and has been widely employed to characterize graphene and its heterostructures [22–24]. In TBG, the moiré-induced band reconstruction modifies the electronic resonance conditions and electron–phonon interaction strength, leading to characteristic changes in the Raman G and 2D modes [25–27]. In particular, theoretical and experimental studies have suggested that the formation of flat bands near the magic angle enhances electron–phonon coupling and results in linewidth broadening and phonon renormalization [28–30]. These features make Raman spectroscopy a promising tool for identifying MATBG and probing its underlying electronic structure. However, in realistic devices, MATBG is typically supported by hexagonal boron nitride (hBN), whose relative rotational alignment introduces an additional moiré potential that further modifies the lattice symmetry and electronic bands. While hBN alignment is known to break graphene sublattice symmetry and strongly influence correlated electronic phases [31,32], whether and how such structural symmetry breaking manifests in Raman signatures remains largely unexplored.

Here, we extend Raman characterization beyond the identification of the magic-angle condition by systematically investigating how the G-mode response evolves with G/hBN alignment. We observe a systematic evolution of the G-mode lineshape and linewidth with increasing G/hBN alignment, providing Raman signatures of substrate-induced symmetry breaking. This alignment-dependent evolution is further enhanced when MATBG becomes aligned with hBN, as confirmed by spatially resolved Raman mapping over large uniform regions. Complementary scanning tunneling microscopy and spectroscopy (STM/S) measurements verify the presence of flat bands and correlated electronic phenomena, and reveal that hBN alignment markedly modifies pseudogap and correlated insulating states through symmetry breaking. Our results demonstrate that Raman spectroscopy not only enables rapid identification of magic-angle and hBN alignment conditions, but also serves as a sensitive probe of symmetry-driven electronic reconstruction in moiré quantum materials.

2 Results

2.1 Raman spectroscopy of TBG

Fig. 1(a) illustrates the heterostructure device employed for Raman characterization. The TBG is assembled via a tear-and-stack method and supported by the few-layer hexagonal boron nitride (hBN) on a SiO_2/Si substrate. The hBN layers provide an atomically flat dielectric environment and suppress extrinsic disorder, thereby preserving the intrinsic electronic and vibrational properties of TBG. Raman measurements were performed in a confocal backscattering geometry using a 532 nm laser focused through a 100× objective, with a laser power of ~3.7 mW at the sample. The scattered light was dispersed by a 600 g/mm grating and detected by a thermoelectrically cooled CCD (−60 °C), enabling high-spectral-resolution measurements of the vibrational modes.

Fig. 1(b) displays the representative Raman spectra of monolayer graphene, Bernal-stacked bilayer graphene, and TBG. We focus on the two prominent features: the G peak (~1580 cm^{-1}), originating from the in-plane E_{2g} optical phonon at the Γ point, and the 2D peak (~2700 cm^{-1}), arising from a double-resonance intervalley scattering process involving transverse optical phonons near the K

Just Accepted

point [22,23]. The primary distinction between monolayer and Bernal bilayer graphene lies in the relative intensity and lineshape of the 2D peak. Monolayer graphene exhibits a single, sharp Lorentzian 2D peak with an intensity typically exceeding that of the G peak, whereas bilayer graphene shows a broadened and split 2D feature due to interlayer band splitting. In contrast to Bernal bilayers, TBG exhibits an angle-dependent 2D lineshape that cannot be simply described by the conventional four-component splitting [33]. Instead, the moiré-induced band reconstruction modifies the resonance conditions, leading to distinct peak broadening and intensity redistribution, thereby providing a spectroscopic signature of twist-induced interlayer coupling [34].

Among the TBG with varying twist angles, we focus particularly on those near 1.1°, commonly referred to as MATBG. Near this angle, the interlayer hybridization and moiré interference reconstruct the Dirac cones into ultra-flat low-energy bands, as illustrated in Fig. 1(c). The dramatically reduced bandwidth enhances the density of states (DOS) and promotes strong electronic correlations, which give rise to correlated insulating states and unconventional superconductivity, making MATBG highly attractive for investigating correlated quantum phenomena. Such flat-band formation also strengthens electron–phonon coupling and modifies the resonance conditions of Raman scattering, leading to phonon renormalization and linewidth broadening that can serve as vibrational signatures of the correlated electronic structure. In Fig. 1(d), we compare two representative devices with twist angles of 1.55° and 1.09°, as determined from the moiré periodicity in the AFM images shown in Figs. 1(e) and 1(f). Their Raman responses are clearly distinct. For the 1.55° device, the G peak is well described by a single Lorentzian profile with a linewidth (Γ_G) of 15.3 cm^{-1}, consistent with a non-magic-angle TBG sample. In contrast, the 1.09° device exhibits a substantially broadened and asymmetric composite G peak, together with a clear splitting into two partially overlapping components, denoted as G^- and G^+. Such G-peak splitting near the magic angle has been reported in previous Raman studies of TBG and attributed to moiré-potential-induced phonon hybridization associated with reduced lattice symmetry [30]. In our spectra, this splitting is accompanied by an evident increase in the effective linewidth of the overall G-peak envelope, reaching $\Gamma_G \approx 19.8$ cm^{-1}. Therefore, beyond resolving the individual G^- and G^+ components, the effective linewidth of the composite G peak provides a convenient and robust experimental metric for identifying the magic-angle regime. Meanwhile, the 2D peak of the 1.09° sample becomes significantly broader, with a linewidth of ~60 cm^{-1}, and evolves toward a more merged single-peak profile, consistent with enhanced electron–phonon coupling near the flat-band condition. Together, these features establish a refined Raman fingerprint of MATBG, in which both G-peak splitting and 2D-peak broadening serve as characteristic signatures.

The Raman anomalies observed in MATBG arise from the combined effects of moiré-induced symmetry reduction and flat-band-enhanced electron–phonon coupling. Once the two graphene layers are twisted away from the high-symmetry AA or AB configurations, the lattice symmetry is lowered; however, away from the magic angle, the moiré potential remains comparatively weak and the G mode still appears as a single broadened peak. Near the magic angle, by contrast, the strengthened moiré potential and the emergence of ultra-flat bands promote phonon hybridization and lift the degeneracy of the G peak, giving rise to the split G^+ and G^- structure. At the same time, the increased DOS enhances electron–phonon coupling, which contributes to the pronounced broadening, particularly of the lower-frequency component. The 2D peak follows a related but distinct evolution: rather than splitting clearly, its multiple double-resonant components become strongly broadened and progressively merge, producing the wide 2D peak observed in the magic-angle sample. These results show that the Raman response near the magic angle is governed not simply by linewidth broadening, but by a coupled evolution of phonon symmetry and electron–phonon interaction.

2.2 The impact of hBN alignment

The above analysis highlights that the Raman response of TBG device is highly sensitive to lattice symmetry and the enhancement of the electronic DOS associated with flat bands. However, the electronic structure and lattice symmetry are governed not only by the interlayer twist within graphene, but also by the underlying hBN substrate. In particular, the relative alignment angle between MATBG and the hBN substrate introduces an additional moiré potential, which can further modify band reconstruction,

Just Accepted

symmetry breaking, and correlation effects. It is therefore natural to expect that the Raman signatures of MATBG may depend sensitively on its rotational alignment with hBN.

Fig. 2(a) presents representative Raman spectra and corresponding peak fittings of six MATBG samples with different G/hBN alignment angles ($\theta_{G/hBN}$). The samples span from largely misaligned configurations ($\theta_{G/hBN}$ > 10°) to nearly fully aligned cases ($\theta_{G/hBN}$ ~ 0°), enabling a systematic investigation of substrate-induced effects. A clear evolution of the G peak lineshape is observed as $\theta_{G/hBN}$ decreases. In misaligned samples ($\theta_{G/hBN}$ > 10°), the G peak exhibits a weakly asymmetric profile that can be described by a dominant component with only a minor shoulder, consistent with the intrinsic two-component character in magic-angle TBG. As the alignment improves ($\theta_{G/hBN}$ ~ 3–5°), the overall linewidth increases and the asymmetry becomes more pronounced, such that the two fitted components (G^+ and G^-) become more evident. In nearly fully aligned samples ($\theta_{G/hBN}$ ~ 0°), the two-component structure is clearly resolved, with both G^+ and G^- significantly broadened, although the G^- component exhibits a lower spectral weight than the G^+ component. This trend is further supported by the statistical analysis of the Γ_G summarized in Fig. 2(b), where Γ_G is the full width at half maximum of the overall G-peak. Within the magic-angle regime, Γ_G increases systematically as the alignment improves. Misaligned samples (blue dots) show Γ_G values around ~19–20 cm^{-1}, consistent with typical magic-angle TBG, whereas partially aligned samples (orange dots) display intermediate linewidths. In contrast, nearly fully aligned samples (purple dots) exhibit significantly enhanced Γ_G, reaching values above 25 cm^{-1}. Notably, this enhancement persists despite variations in $\theta_{G/G}$ among different samples, indicating that the increase in Γ_G cannot be attributed solely to twist-angle variations, but instead arises from the alignment with the hBN substrate. Therefore, while the G peak linewidth has previously been used as a practical reference for identifying the magic-angle condition, our results show that, within the magic-angle regime, the same effective linewidth further provides a sensitive indicator of G/hBN alignment.

This systematic evolution indicates that hBN alignment enhances the lifting of the E_{2g} phonon degeneracy beyond that induced by the G/G moiré alone. Notably, the linewidth increase is particularly pronounced for the lower-frequency component (G^-), consistent with enhanced electron–phonon coupling in the flat-band regime. This behavior can be understood as a consequence of the additional moiré potential introduced by the hBN substrate. As $\theta_{G/hBN}$ approaches zero, the long-wavelength G/hBN moiré becomes comparable to the G/G moiré, leading to enhanced sublattice symmetry breaking and further reduction of the system symmetry. The resulting symmetry breaking promotes phonon hybridization and strengthens electron–phonon interaction, thereby reinforcing the asymmetric two-component lineshape and the overall broadening of the G peak. In addition, the G/hBN moiré potential can further reconstruct the flat-band electronic structure by modifying the band dispersion, which is expected to alter electronic screening and enhance electron–phonon coupling. These combined effects consistently explain why nearly fully aligned MATBG exhibits substantially larger Γ_G than misaligned samples, even within the same magic-angle regime. These results demonstrate that hBN alignment provides an effective tuning parameter for the Raman response of MATBG, enabling direct spectroscopic access to symmetry breaking in moiré systems.

We further employed spatially resolved Raman measurements to verify the generality of the above conclusion. Two MATBG samples with large, uniform regions were selected, and their large-area AFM topographies are shown in Figs. 2(c) and 2(e). The MATBG region is enclosed by gold electrodes to enable subsequent STM measurements. From the topographical measurements, we determined the corresponding $\theta_{G/G}$ and $\theta_{G/hBN}$ for each sample, identifying one as hBN-misaligned and the other as nearly fully aligned, with uniform twist angles over extended areas. Real-space Raman measurements were performed within the regions indicated by the dashed red boxes, from which spatial maps of Γ_G were extracted, as shown in Figs. 2(d) and 2(f). The misaligned sample exhibits a Γ_G distribution around ~20 cm^{-1}, whereas the aligned sample shows a distribution around ~25 cm^{-1}. This clear spatial contrast further confirms that the broadening of Γ_G induced by hBN alignment is not incidental, but instead represents a robust, structure-dependent effect.

2.3 STM characterization of the correlated electronic states

To further substantiate that the Raman measurements

Just Accepted

establish a direct connection between the Raman signatures and the structural properties as well as correlated electronic states of TBG, we performed STM/S measurements on the same set of samples. Three devices with $\theta_{G/G}$ near the magic angle but markedly different $\theta_{G/hBN}$ were selected as the examples. The STM topographic images of these samples shown in Figs. 3(a)–3(c) clearly resolve two distinct moiré patterns: the triangular lattice associated with the G/G moiré and the hexagonal lattice arising from the G/hBN moiré. As $\theta_{G/hBN}$ approaches zero, the G/hBN moiré period increases progressively and eventually becomes comparable to that of the G/G moiré, forming an intertwined super-moiré structure.

By tuning the carrier density via the back gate and performing dI/dV measurements, we probed the electronic band characteristics of these samples. Fig. 3(d) shows representative dI/dV spectra of MATBG at full electron and hole filling, as well as at the charge neutrality point, where the two pronounced peaks correspond to the conduction and valence flat bands [35–37]. Each flat band has fourfold degeneracy, corresponding to isospin (spin and valley) degrees of freedom [38–40]. Therefore, we determine the filling factor as ν = -4 when two flat bands are both empty and ν = +4 when two flat bands are fully occupied. Following this criterion, all the intermediate filling factors ν could be determined precisely. As shown in Figs. 3(e)-3(g), by tuning the gate voltage, the evolution of the spectra reveals a series of characteristic correlation-driven features. The cascade feature, highlighted by the black dashed lines, manifests as a sequence of abrupt spectral weight redistribution and band shifts as a function of filling [41,42]. This behavior is further supported by the dI/dV waterfall plot shown in Figs. 3(h)–3(j), where the peak positions (indicated by colored triangles) exhibit discrete jumps near each integer filling rather than continuous evolution. As schematically illustrated in Fig. 3(k), such cascade-like behavior reflects interaction-driven band renormalization, in which electron correlations reorganize the flat-band spectrum upon successive filling. In addition, a pseudogap feature emerges near the Fermi level in filling ranges, as indicated by the green arrows. This feature appears as a partial suppression of the density of states and is clearly resolved in the dI/dV spectra highlighted by green dashed boxes in Figs. 3(h) and 3(i), where a depletion of spectral weight develops without forming a full gap. Such behavior has been reported previously as a precursor state associated with superconductivity [17,43,44]. Moreover, the red arrows indicate pronounced suppression of tunneling conductance at integer fillings, corresponding to correlated insulating states arising from strong electron–electron interactions within the flat bands. In Fig. 3(j), these states appear as well-defined gaps that persist over a finite range of bias (red curves), providing clear spectroscopic signatures of interaction-driven insulating phases. These features demonstrate the presence of the characteristic strong correlation phenomena of MATBG in all measured samples.

A comparison among the different samples reveals that the alignment with the hBN substrate markedly influences these correlated electronic states. In particular, the pseudogap feature is observed in the misaligned and partially aligned MATBG samples but becomes absent in the fully aligned device. In contrast, correlated insulating states at integer fillings emerge clearly in the partially aligned sample and become further enhanced upon full alignment, while they are largely suppressed in the fully misaligned case. These differences in correlated phenomena are closely linked to the symmetry breaking induced by hBN alignment. In aligned MATBG, the graphene sublattice symmetry—namely the C_2 symmetry—is broken, which gaps the Dirac points. Combined with the strong electron–electron interactions in the flat bands, this enables the emergence of correlated insulating states at integer fillings even at zero magnetic field. However, in MATBG that preserves C_2 symmetry, correlated insulating gaps at integer fillings can only be observed under a finite magnetic field [11,13]. Meanwhile, superconductivity and pseudogap features have been reported in previous transport [9,10] and STM [17] studies to be suppressed in hBN-aligned MATBG. Although direct evidence remains limited, this behavior is believed to originate from the breaking of C_2 symmetry. These results demonstrate that symmetry breaking imposed by hBN alignment plays a decisive role in shaping the band structure and correlated electronic phases of MATBG.

3 Conclusions

In summary, we demonstrate that Raman spectroscopy provides a direct and sensitive probe of symmetry breaking in magic-angle twisted bilayer graphene. Near the magic angle, the G peak evolves from a single-component profile

Just Accepted

into a split two-component structure, reflecting the lifting of the E_{2g} phonon degeneracy and the emergence of flat-band–enhanced electron–phonon coupling. Building on this, we show that alignment with the hBN substrate further enhances the asymmetric two-component lineshape and linewidth of the G peak, arising from the additional moiré potential that strengthens sublattice symmetry breaking and modifies the electronic structure. Spatially resolved Raman measurements confirm that this enhancement is uniform over large areas, indicating that it is an intrinsic effect of the heterostructure rather than local disorder. Guided by the Raman identification, STM/S measurements reveal the characteristic cascade, pseudogap, and correlated insulating states in all samples, establishing a direct correspondence between Raman signatures, structural symmetry, and correlated electronic phases. Compared with scanning probe techniques such as AFM and STM, which typically require time-consuming high-resolution measurements, Raman spectroscopy enables rapid, non-destructive, and contact-free mapping over relatively large areas. The G-mode lineshape and linewidth identified here therefore serve as practical Raman fingerprints for identifying magic-angle and hBN-aligned regions prior to further microscopic characterization. Our results establish Raman spectroscopy as a rapid, non-destructive tool for identifying both magic-angle conditions and substrate-induced symmetry breaking, and provide a unified framework linking lattice symmetry, moiré potentials, and strongly correlated phenomena in twisted graphene systems.

4 Methods

4.1 Raman spectroscopy

Raman measurements were performed using a WITec confocal Raman system in a backscattering geometry. A 532 nm laser with a power of approximately 3.7 mW was focused onto the sample through a 100× objective (NA = 0.9). The scattered light was dispersed using a 600 grooves/mm grating and detected by a CCD cooled to −60 °C. Each spectrum was acquired with an integration time of 8 s and averaged over two accumulations.

4.2 STM/S

STM/STS measurements were performed at 4.4 K under ultrahigh-vacuum conditions ($< 1 \times 10^{-10}$ mbar) using electrochemically etched tungsten tips calibrated on a Cu(111) surface. Topographic images were acquired in constant-current mode. The dI/dV spectra and maps were measured using standard lock-in detection with a 1 mV AC modulation at 711 Hz applied to the DC sample bias.

4.3 Identification of the twist angle

The G/G and G/hBN moiré patterns were distinguished from the AFM and STM topographic images, and their local moiré wavelengths were measured separately. The corresponding twist angles were calculated using

$$\theta = \arccos\left[1 - \frac{\frac{(1+\delta)^2 a^2}{\lambda^2} - \delta^2}{2(1+\delta)}\right]$$

where a = 0.246 nm is the graphene lattice constant, λ is the measured moiré wavelength, and δ is the relative lattice mismatch. For the G/G moiré δ = 0, whereas for the G/hBN moiré δ = 0.018.

Data availability

The data supporting the key findings of this study are available from the corresponding authors upon request.

Acknowledgements

This work was supported by the Fundings from the National Natural Science Foundation of China (Grants No. 12474477, No. 12550405 and No. 61888102); the Beijing Outstanding Young Scientist Program; Fundamental Research Funds for the Central Universities; Scientific Research Innovation Capability Support Project for Young Faculty (SRICSPYF-Chinese Academy of Sciences; the EMEXT ElementZY2025071); the robotic AI-Scientist platform of Strategy Initiative to Form Core Research Center through Grant No. JPMXP0112101001.

Author contribution statement

J.M. and Y.J. conceived and supervised the experiments. Y.H. was responsible for device fabrication. Y.H. and Y.W. conducted the STM measurements. Y.H. and J.J. analyzed the experimental data. K.W. and T.T. provided the hBN crystals. Y.H., J.J., Y.W., Y.J., and J.M. participated in discussions of the

Just Accepted

results and contributed to the manuscript preparation.

References

[1] Geim, A. K.; Grigorieva, I. V. Van der Waals heterostructures. Nature 2013, 499, 419-425.

[2] Novoselov, K. S.; Mishchenko, A.; Carvalho, A.; Castro Neto, A. H. 2D materials and van der Waals heterostructures. Science 2016, 353, aac9439.

[3] Andrei, E. Y.; MacDonald, A. H. Graphene bilayers with a twist. Nat. Mater. 2020, 19, 1265-1275.

[4] Balents, L.; Dean, C. R.; Efetov, D. K.; Young, A. F. Superconductivity and strong correlations in moiré flat bands. Nat. Phys. 2020, 16, 725-733.

[5] Bistritzer, R.; MacDonald, A. H. Moiré bands in twisted double-layer graphene. Proc. Natl. Acad. Sci. 2011, 108, 12233-12237.

[6] Suárez Morell, E.; Correa, J. D.; Vargas, P.; Pacheco, M.; Barticevic, Z. Flat bands in slightly twisted bilayer graphene: Tight-binding calculations. Phys. Rev. B 2010, 82, 121407.

[7] Shallcross, S.; Sharma, S.; Kandelaki, E.; Pankratov, O. A. Electronic structure of turbostratic graphene. Phys. Rev. B 2010, 81, 165105.

[8] Cao, Y. et al. Correlated insulator behaviour at half-filling in magic-angle graphene superlattices. Nature 2018, 556, 80-84.

[9] Sharpe, A. L.; Fox, E. J.; Barnard, A. W.; Finney, J.; Watanabe, K.; Taniguchi, T.; Kastner, M. A.; Goldhaber-Gordon, D. Emergent ferromagnetism near three-quarters filling in twisted bilayer graphene. Science 2019, 365, 605-608.

[10] Serlin, M.; Tschirhart, C. L.; Polshyn, H.; Zhang, Y.; Zhu, J.; Watanabe, K.; Taniguchi, T.; Balents, L.; Young, A. F. Intrinsic quantized anomalous Hall effect in a moiré heterostructure. Science 2020, 367, 900-903.

[11] Wu, S.; Zhang, Z.; Watanabe, K.; Taniguchi, T.; Andrei, E. Y. Chern insulators, van Hove singularities and topological flat bands in magic-angle twisted bilayer graphene. Nat. Mater. 2021, 20, 488-494.

[12] Stepanov, P.; Xie, M.; Taniguchi, T.; Watanabe, K.; Lu, X.; MacDonald, A. H.; Bernevig, B. A.; Efetov, D. K. Competing Zero-Field Chern Insulators in Superconducting Twisted Bilayer Graphene. Phys. Rev. Lett. 2021, 127, 197701.

[13] Nuckolls, K. P.; Oh, M.; Wong, D.; Lian, B.; Watanabe, K.; Taniguchi, T.; Bernevig, B. A.; Yazdani, A. Strongly correlated Chern insulators in magic-angle twisted bilayer graphene. Nature 2020, 588, 610-615.

[14] Cao, Y.; Fatemi, V.; Fang, S.; Watanabe, K.; Taniguchi, T.; Kaxiras, E.; Jarillo-Herrero, P. Unconventional superconductivity in magic-angle graphene superlattices. Nature 2018, 556, 43-50.

[15] Lu, X. et al. Superconductors, orbital magnets and correlated states in magic-angle bilayer graphene. Nature 2019, 574, 653-657.

[16] Yankowitz, M.; Chen, S.; Polshyn, H.; Zhang, Y.; Watanabe, K.; Taniguchi, T.; Graf, D.; Young, A. F.; Dean, C. R. Tuning superconductivity in twisted bilayer graphene. Science 2019, 363, 1059-1064.

[17] Oh, M.; Nuckolls, K. P.; Wong, D.; Lee, R. L.; Liu, X.; Watanabe, K.; Taniguchi, T.; Yazdani, A. Evidence for unconventional superconductivity in twisted bilayer graphene. Nature 2021, 600, 240-245.

[18] Das, I.; Lu, X.; Herzog-Arbeitman, J.; Song, Z.-D.; Watanabe, K.; Taniguchi, T.; Bernevig, B. A.; Efetov, D. K. Symmetry-broken Chern insulators and Rashba-like Landau-level crossings in magic-angle bilayer graphene. Nat. Phys. 2021, 17, 710-714.

[19] Saito, Y.; Ge, J.; Rademaker, L.; Watanabe, K.; Taniguchi, T.; Abanin, D. A.; Young, A. F. Hofstadter subband ferromagnetism and symmetry-broken Chern insulators in twisted bilayer graphene. Nat. Phys. 2021, 17, 478-481.

[20] Jiang, Y.; Lai, X.; Watanabe, K.; Taniguchi, T.; Haule, K.; Mao, J.; Andrei, E. Y. Charge order and broken rotational symmetry in magic-angle twisted bilayer graphene. Nature 2019, 573, 91-95.

[21] He, M. et al. Strongly interacting Hofstadter states in magic-angle twisted bilayer graphene. Nat. Phys. 2025, 21, 1380-1386.

[22] Ferrari, A. C. et al. Raman Spectrum of Graphene and Graphene Layers. Phys. Rev. Lett. 2006, 97, 187401.

[23] Ferrari, A. C.; Basko, D. M. Raman spectroscopy as a versatile tool for studying the properties of graphene. Nat. Nanotechnol. 2013, 8, 235-246.

[24] Cançado, L. G.; Jorio, A.; Ferreira, E. H. M.; Stavale, F.; Achete, C. A.; Capaz, R. B.; Moutinho, M. V. O.; Lombardo, A.; Kulmala, T. S.; Ferrari, A. C. Quantifying Defects in Graphene via Raman Spectroscopy at Different Excitation Energies. Nano Lett. 2011, 11, 3190-3196.

[25] Kim, K.; Coh, S.; Tan, L. Z.; Regan, W.; Yuk, J. M.; Chatterjee, E.; Crommie, M. F.; Cohen, M. L.; Louie, S. G.; Zettl, A. Raman Spectroscopy Study of Rotated Double-Layer Graphene: Misorientation-Angle Dependence of Electronic Structure. Phys. Rev. Lett. 2012, 108, 246103.

[26] Schäpers, A. et al. Raman imaging of twist angle variations in twisted bilayer graphene at intermediate angles. 2D Mater. 2022, 9, 045009.

[27] Barbosa, T. C.; Gadelha, A. C.; Ohlberg, D. A. A.; Watanabe, K.; Taniguchi, T.; Medeiros-Ribeiro, G.; Jorio, A.; Campos, L. C. Raman spectra of twisted bilayer graphene close to the magic angle. 2D Mater. 2022, 9, 025007.

[28] Moutinho, M. V. O.; Venezuela, P.; Pimenta, M. A. Raman Spectroscopy of Twisted Bilayer Graphene. C 2021, 7, 10.

Just Accepted

[29] Gadelha, A. C.; Nguyen, V.-H.; Neto, E. G. S.; Santana, F.; Raschke, M. B.; Lamparski, M.; Meunier, V.; Charlier, J.-C.; Jorio, A. Electron–Phonon Coupling in a Magic-Angle Twisted-Bilayer Graphene Device from Gate-Dependent Raman Spectroscopy and Atomistic Modeling. Nano Lett. 2022, 22, 6069-6074.

[30] Solanki, D.; Watanabe, K.; Taniguchi, T.; Sood, A. K.; Das, A. Anomalies in G and 2 D Raman modes of twisted bilayer graphene near the magic angle. Phys. Rev. B 2025, 112, 045412.

[31] Yankowitz, M.; Xue, J.; Cormode, D.; Sanchez-Yamagishi, J. D.; Watanabe, K.; Taniguchi, T.; Jarillo-Herrero, P.; Jacquod, P.; LeRoy, B. J. Emergence of superlattice Dirac points in graphene on hexagonal boron nitride. Nat. Phys. 2012, 8, 382-386.

[32] Hunt, B. et al. Massive Dirac Fermions and Hofstadter Butterfly in a van der Waals Heterostructure. Science 2013, 340, 1427-1430.

[33] Havener, R. W.; Zhuang, H.; Brown, L.; Hennig, R. G.; Park, J. Angle-Resolved Raman Imaging of Interlayer Rotations and Interactions in Twisted Bilayer Graphene. Nano Lett. 2012, 12, 3162-3167.

[34] Carozo, V. et al. Resonance effects on the Raman spectra of graphene superlattices. Phys. Rev. B 2013, 88, 085401.

[35] Li, G.; Luican, A.; Lopes dos Santos, J. M. B.; Castro Neto, A. H.; Reina, A.; Kong, J.; Andrei, E. Y. Observation of Van Hove singularities in twisted graphene layers. Nat. Phys. 2010, 6, 109-113.

[36] Kerelsky, A. et al. Maximized electron interactions at the magic angle in twisted bilayer graphene. Nature 2019, 572, 95-100.

[37] Choi, Y. et al. Electronic correlations in twisted bilayer graphene near the magic angle. Nat. Phys. 2019, 15, 1174-1180.

[38] Song, Y. J. et al. High-resolution tunnelling spectroscopy of a graphene quartet. Nature 2010, 467, 185-189.

[39] Young, A. F.; Dean, C. R.; Wang, L.; Ren, H.; Cadden-Zimansky, P.; Watanabe, K.; Taniguchi, T.; Hone, J.; Shepard, K. L.; Kim, P. Spin and valley quantum Hall ferromagnetism in graphene. Nat. Phys. 2012, 8, 550-556.

[40] Freitag, N. M. et al. Large tunable valley splitting in edge-free graphene quantum dots on boron nitride. Nat. Nanotechnol. 2018, 13, 392-397.

[41] Wong, D.; Nuckolls, K. P.; Oh, M.; Lian, B.; Xie, Y.; Jeon, S.; Watanabe, K.; Taniguchi, T.; Bernevig, B. A.; Yazdani, A. Cascade of electronic transitions in magic-angle twisted bilayer graphene. Nature 2020, 582, 198-202.

[42] Zondiner, U. et al. Cascade of phase transitions and Dirac revivals in magic-angle graphene. Nature 2020, 582, 203-208.

[43] Park, J. M.; Sun, S.; Watanabe, K.; Taniguchi, T.; Jarillo-Herrero, P. Experimental evidence for nodal superconducting gap in moiré graphene. Science 2026, 391, 79-83.

[44] Han, Y.; Wang, Y.; Xue, Y.; Shi, J.; Wang, X.; Watanabe, K.; Taniguchi, T.; Kang, J.; Jiang, Y.; Mao, J. Spectral signature of periodic modulation and shifting of pseudogap state in moiré system. Nat. Commun. 2026, 17, 4939.

Just Accepted

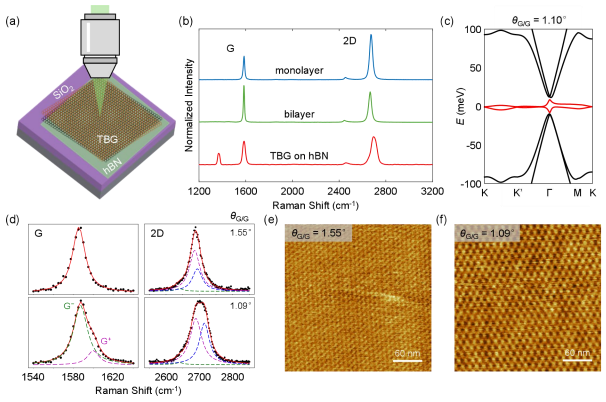


Figure 1 (a) The schematic of the TBG device and Raman spectroscopy setup. (b) Raman spectra of monolayer graphene, Bernal bilayer graphene and TBG device. (c) Band structure calculated using a continuum model for MATBG ($\theta = 1.10°$), with red color highlighting two flat bands. (d) G and 2D peak Raman spectra and the corresponding fit for 1.55° and 1.09° TBG samples. Experimental data are represented by black dots. The dotted lines indicate the individual Lorentzian fits, and the solid red line shows the overall fit. (e), (f) AFM imaging of the moiré superlattices in the two TBG devices.

Just Accepted

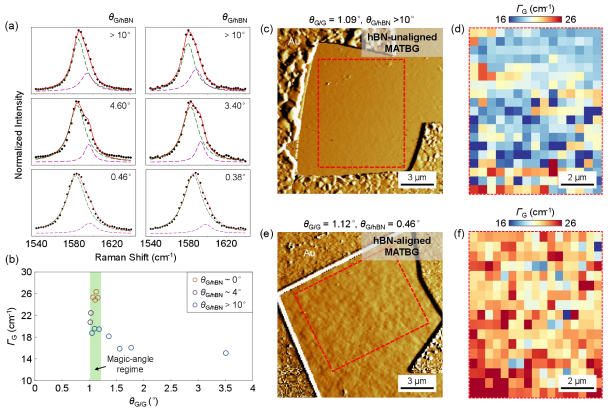


Figure 2 (a) G peak Raman spectra and the corresponding fit for MATBG devices with different hBN alignment. Experimental data are represented by black dots. The dotted lines indicate the individual Lorentzian fits, and the solid red line shows the overall fit. (b) G peak full width at half maximum (Γ_G) dependence on the G/G twist angle. The colored circles correspond to different categories of G/hBN twist angles. (c) Large-area AFM topography for one hBN-misaligned MATBG device. (d) The spatial distribution of Γ_G extracted from the Raman mapping within the red boxed region in (c). (e) Large-area AFM topography for one hBN-aligned MATBG device. (f) The spatial distribution of Γ_G extracted from the Raman mapping within the red boxed region in (e).

Just Accepted

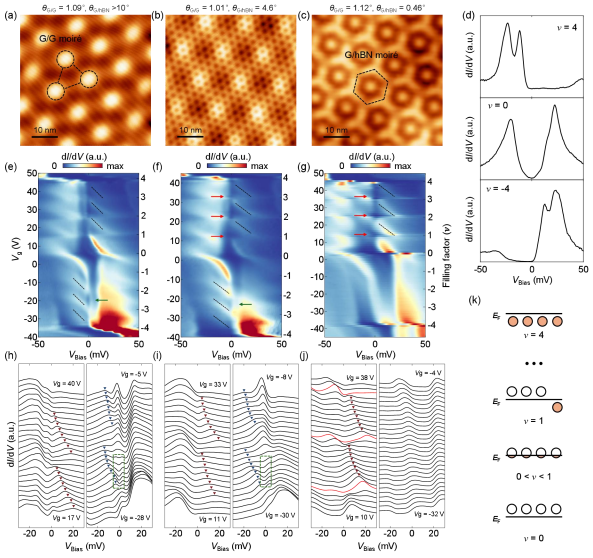


Figure 3 (a)-(c) STM topography of three MATBG devices with different hBN alignment (V_{Bias} = -100 mV, I = 50 pA). (d) Representative dI/dV spectra for the fully occupied band (ν = +4), charge neutral point (ν = 0), and fully empty band (ν = -4). (e)-(g) Gate-dependent dI/dV spectra taken at AA stacking region of G/G moiré for each MATBG device (V_{Bias} = -50mV, I = 300 pA). The black dashed lines mark the cascade features, the green arrows indicate the pseudogap features, and the red arrows highlight the correlated insulating features. (h)-(j) dI/dV waterfall plots for each MATBG device. The red (blue) triangles mark peaks corresponding to the cascade features at electron (hole) doping side. The green dashed boxes indicate the pseudogap feature. The red curves in (j) indicate the emergence of the correlated insulating states. (k) Schematic of flat band filling. Circles denote the fourfold-degenerate flat-band components, with filled circles representing occupied states below E_F. At each integer filling, electron correlations drive band reconstruction, fully filling one subband and shifting the remaining states, giving rise to the cascade-like evolution in dI/dV spectra.

Just Accepted

Electronic Supplementary Material

Raman fingerprints of symmetry breaking and correlated electronic states in magic-angle twisted bilayer graphene

Yingzhuo Han[1], Junnan Jiang[2], Yingbo Wang[1], Kenji Watanabe[3], Takashi Taniguchi[4], Yuhang Jiang[2*], Jinhai Mao[1]*

1. School of Physical Sciences, University of Chinese Academy of Sciences, Beijing 100049, China

2. College of Materials Science and Optoelectronic Technology, Center of Materials Science and Optoelectronics Engineering, University of Chinese Academy of Sciences, Beijing 100049, China

3. Research Center for Electronic and Optical Materials, National Institute for Materials Science, Tsukuba 305-0044, Japan

4. International Center for Materials Nanoarchitectonics, National Institute for Materials Science, Tsukuba 305-0044, Japan

Supporting information to https://doi.org/10.26599/NR.2026.94909237

Just Accepted

1. Band structure calculation for MATBG

We calculated the electronic band structure of magic-angle twisted bilayer graphene (MATBG) using the Bistritzer–MacDonald continuum model[1]. In this framework, the moiré potential folds the original graphene bands into a reduced moiré Brillouin zone (MBZ), which retains a hexagonal geometry. The reciprocal lattice vectors of the moiré superlattice are given by $\mathbf{b}_1^m = \sqrt{3}|\Delta K|\left(\frac{1}{2}, -\frac{\sqrt{3}}{2}\right)$, $\mathbf{b}_2^m = \sqrt{3}|\Delta K|\left(\frac{1}{2}, \frac{\sqrt{3}}{2}\right)$, where $\Delta K = 2|K|sin\,(\theta/2)$ is the momentum-space separation between the Dirac points of the two graphene layers. Correspondingly, the moiré real lattice can be spanned by $\mathbf{a}_1^m = \frac{4\pi}{3|\Delta K|}\left(\frac{\sqrt{3}}{2}, -\frac{1}{2}\right)$ and $\mathbf{a}_2^m = \frac{4\pi}{3|\Delta K|}\left(\frac{\sqrt{3}}{2}, \frac{1}{2}\right)$, and the unit cell of moiré lattice has area $A_{u.c} = \left|\mathbf{a}_1^m \times \mathbf{a}_2^m\right| = \frac{3\sqrt{3}d^2}{8\sin^2(\theta/2)}$.

The low energy Dirac Hamiltonian can be written as $H = H_{\mathrm{MG1}} + H_{\mathrm{MG2}} + H_{\mathrm{M}}$, where H_{MG1} and H_{MG2} represents two individual monolayer graphene layers and H_{M} represents the coupling between two layers. For each layer the Hamiltonian can

be written by the momentum $\mathbf{q} = \mathbf{k} - K_l$ ($l = \mathrm{MG1}, MG2$). And for each momentum $\mathbf{k}$ in the MBZ, the base of the Hamiltonian matrix are Bloch states $|l, \mathbf{k} + m_1\mathbf{b}_1^m + m_2\,\mathbf{b}_2^m, \tau\rangle$, where m_1 and m_2 are integers and $\tau = A, B$ denotes the sublattices. The twist angle in our experiment is $\theta = 1.09°$.

The Hamiltonian for the monolayer graphene is

$$H_l = \sum_{\mathbf{k}} \Psi_l^\dagger(\mathbf{k})\, \hbar v_F |\mathbf{q}| \begin{pmatrix} 0 & e^{-i(\theta_{\mathbf{q}} - \theta_l)} \\ e^{i(\theta_{\mathbf{q}} - \theta_l)} & 0 \end{pmatrix} \Psi_l(\mathbf{k}),$$

where $\Psi_l^\dagger(\mathbf{k}) = \left(a_l^\dagger(\mathbf{k}), b_l^\dagger(\mathbf{k})\right)$ and $a_l^\dagger(\mathbf{k})$ and $b_l^\dagger(\mathbf{k})$ are the electron operators for sublattice sites, $v_F = 10^6 m/s$ is the fermi velocity of graphene, $\theta_{\mathrm{MG1}} = -\frac{\theta}{2}$, $\theta_{\mathrm{MG2}} = \frac{\theta}{2}$, and $\theta_{\mathbf{q}}$ the angle that the momentum $\mathbf{q}$ makes with the x axis.

The Hamiltonian for the interlayer moiré tunneling is

$$H_{\mathrm{M}} = \sum_{\mathbf{k}} \sum_{j=0,\,1,\,2} \left(a_{\mathrm{MG}}^\dagger(\mathbf{k}), b_{\mathrm{MG}}^\dagger(\mathbf{k})\right) T_{\mathbf{Q}_j} \begin{pmatrix} a_{\mathrm{BG1}}^\dagger(\mathbf{k} + \mathbf{Q}_j) \\ b_{\mathrm{BG1}}^\dagger(\mathbf{k} + \mathbf{Q}_j) \end{pmatrix} + h.c.$$

where $\mathbf{Q_0} = (0,0)$, $\mathbf{Q_1} = \mathbf{b}_2^m$, $\mathbf{Q_2} = -\mathbf{b}_1^m$, and the corresponding tunneling matrix are

$$T_{\mathbf{Q_0}} = \frac{t_\perp(|K|)}{A_{u.c}} \begin{pmatrix} 1 & 1 \\ 1 & 1 \end{pmatrix},$$

$$T_{\mathbf{Q_1}} = \frac{t_\perp(|K|)}{A_{u.c}} \begin{pmatrix} e^{-i\phi} & 1 \\ e^{i\phi} & e^{-i\phi} \end{pmatrix},$$

$$T_{\mathbf{Q_2}} = \frac{t_\perp(|K|)}{A_{u.c}} \begin{pmatrix} e^{i\phi} & 1 \\ e^{-i\phi} & e^{i\phi} \end{pmatrix},$$

where $t_\perp(|K|) \cong 0.58$ eV Å^2 is the interlayer tunneling term[2] and $\phi = \frac{2\pi}{3}$.

2. Lorentzian fitting of the G peak

The Raman spectra were fitted using Lorentzian functions superimposed on a linear background to quantitatively extract the peak position, full width at half maximum (FWHM), and integrated intensity of each Raman mode. For the G peak, spectra displaying a single symmetric profile were fitted with one Lorentzian component, whereas spectra showing a clear asymmetric lineshape or resolvable shoulder were fitted with two Lorentzian components, denoted as G^- and G^+. The

Just Accepted

number of components was determined by the experimentally resolved spectral features and further checked by the fitting residuals to avoid over-parameterization. The extracted peak parameters were then used for the statistical analysis of the twist-angle- and hBN-alignment-dependent Raman response.

3. STM measurement of the MATBG device

Fig. S3(a) illustrates the device configuration used for the STM measurements of MATBG. The MATBG was assembled on a hexagonal boron nitride (hBN) substrate and placed on a SiO_2 /Si wafer. The highly doped Si substrate served as a global back gate, allowing the carrier density in MATBG to be tuned by the gate voltage V_g. During the STM measurements, the STM tip was electrically grounded, while the bias voltage was applied to the graphene sample.

The STM experiments were performed in an ultrahigh-vacuum environment with a base pressure better than 1×10^{-10} mbar and base temperature 4.4 K. The STM tips were calibrated on a clean Cu(111) surface before the measurements. Topographic images were acquired in constant-current mode. Differential conductance (dI/dV) spectra were measured using a standard lock-in technique, with an AC modulation of 1 mV at 711 Hz added to the DC sample bias.

Large-area STM topographies of representative hBN-unaligned and hBN-aligned MATBG devices are shown in Fig. S3(c, d). The images were taken over a field of view of 400 nm, allowing us to examine the spatial uniformity of the moiré structures over extended regions. Both images exhibit well-defined moiré patterns across the full imaging area, indicating that the structural characteristics are not limited to local regions but remain uniform over hundreds of nanometers.

Just Accepted

Device	$\theta_{G/G}$ (°)	$\theta_{G/hBN}$ (°)	Γ_G (cm^{-1})	Γ_{2D} (cm^{-1})
1	3.5	>10	15.3	35.9
2	1.76	>10	16.3	50.2
3	1.55	>10	16.1	52.7
4	1.35	>10	18.4	53.8
5	1.04	>10	19.0	60.3
6	1.09	>10	19.8	60.8
7	1.05	>10	19.8	58.0
8	1.17	>10	19.7	56.9
9	1.01	4.60	21.0	60.6
10	1.02	3.40	22.7	58.1
11	1.10	0.46	25.1	62.5
12	1.12	0.38	26.6	62.0
13	1.15	0.50	25.5	64.2
14	1.06	0.25	25.6	62.3

Table S1 Summary of $\theta_{G/G}$, $\theta_{G/hBN}$, Γ_G, and Γ_{2D} for the measured devices. Red values denote G/G twist angles close to the magic angle and G/hBN twist angles close to zero. The data show that Γ_G is broadened near the magic angle and is further enhanced upon hBN alignment.

Just Accepted

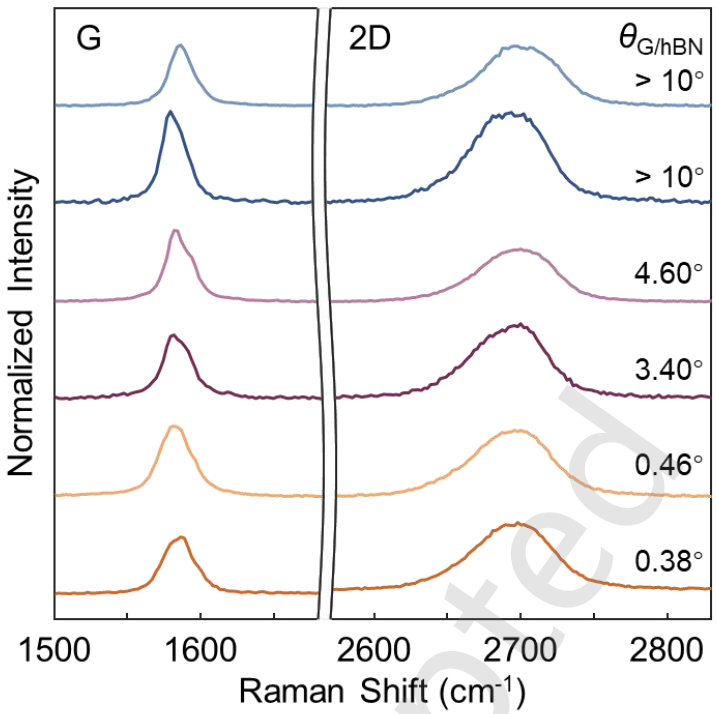


Fig. S1 Raman spectra showing the G and 2D peaks of the MATBG devices presented in main text Fig. 2. The spectra reveal a clear broadening trend of the G peak as $\theta_{G/hBN}$ decreases, indicating the enhanced influence of the hBN-induced moiré potential on the Raman spectra.

Just Accepted

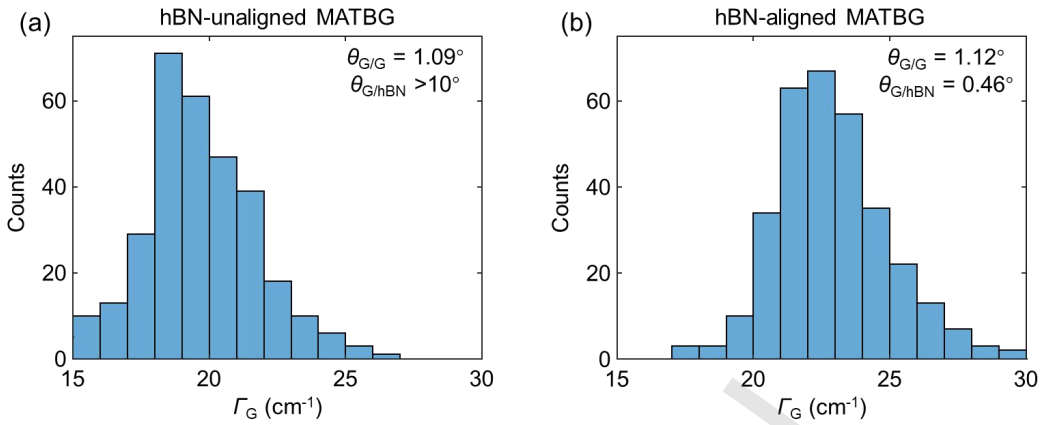


Fig. S2 (a), (b) Histograms of Γ_G extracted from the Raman maps shown in main text Figs. 2d and 2f. The hBN-unaligned MATBG device shows a Γ_G distribution centered around 19 cm^{-1}, whereas the hBN-aligned device exhibits a distribution mainly around 23 cm^{-1}. This comparison further confirms the enhanced G-peak broadening induced by graphene–hBN alignment.

Just Accepted

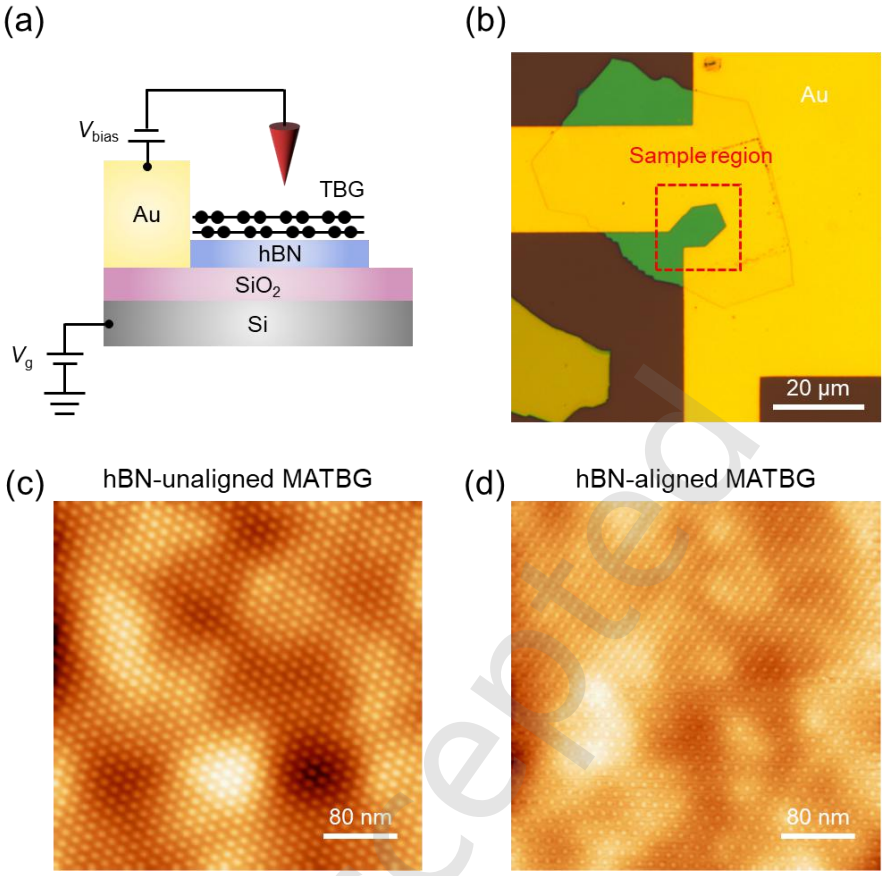


Fig. S3 (a) Schematic illustration of the MATBG device used for STM measurements. (b) Optical microscope image of a representative MATBG device. (c), (d) Representative large-area STM topographies of hBN-unaligned and hBN-aligned MATBG devices, respectively. The moiré structural features are uniformly distributed over an extended real-space region, confirming the large-scale structural homogeneity of the devices.

Just Accepted

References

(1) Bistritzer, R.; MacDonald, A. H. Moiré Bands in Twisted Double-Layer Graphene. Proc. Natl. Acad. Sci. 2011, 108 (30), 12233–12237. https://doi.org/10.1073/pnas.1108174108.

(2) Kuzmenko, A. B.; Crassee, I.; van der Marel, D.; Blake, P.; Novoselov, K. S. Determination of the Gate-Tunable Band Gap and Tight-Binding Parameters in Bilayer Graphene Using Infrared Spectroscopy. Phys. Rev. B 2009, 80 (16), 165406. https://doi.org/10.1103/PhysRevB.80.165406.

Just Accepted